JOURNAL OF AIRCRAFT
Vol. 29, No. 6, Nov.–Dec. 1992

Numerical Modeling of an Advanced Pneumatic Impulse Ice Protection System for Aircraft

Subramaniam Ramamurthy,* Theo G. Keith Jr.,† and Kenneth J. De Witt‡
University of Toledo, Toledo, Ohio 43606
and
James C. Putt,§ Charles A. Martin,¶ and Kevin L. Leffel**
B.F. Goodrich Aerospace Division, Uniontown, Ohio 44685

The development of a numerical model of an advanced pneumatic impulse ice protection system for aircraft is described in this paper. A time-dependent, compressible flow model for internal duct flow is used to model the ice protection system, also known as PIIP. The model incorporates a high resolution shock capturing method, essentially nonoscillatory (ENO) scheme with subcell resolution (SR) and characteristic direction (CD). The model consists of a constant pressure reservoir, a variable area valve, and a tube section that expands due to the passage of a shockwave. A grid generation scheme is used to account for the size of the system. The model is analyzed for different inlet and exit boundary conditions. Preliminary results are obtained for a range of compressor pressures and the model is shown to give results of practical use. The paper also recommends a suitable operating pressure for the compressor.

Nomenclature

A = cross-sectional area
$\boldsymbol{A}$ = Jacobian of the flux $\boldsymbol{F}$
c = speed of sound
E = total internal energy per unit volume
e = specific internal energy
$\boldsymbol{F}$ = inviscid flux vector
f = approximate numerical flux
h = correction term for cell with discontinuity
$\boldsymbol{L}$ = polynomial of degree (r-1) for rth order accurate scheme
l = elements of left-eigenvector of $\boldsymbol{A}$
M = Mach number
p = pressure
R = reconstructed value of v
r = elements of right-eigenvector of $\boldsymbol{A}$
$\boldsymbol{S}$ = source vector
T = temperature
$\boldsymbol{T}$ = right-eigenvector of $\boldsymbol{A}$
t = time
$\boldsymbol{U}$ = vector of conserved variables
u = axial velocity
v = approximate solution
w = characteristic variable
x = axial distance
γ = ratio of specific heats
Δ = increment
$\boldsymbol{\Lambda}$ = matrix of eigenvalues of the matrix $\boldsymbol{A}$
λ = eigenvalues of $\boldsymbol{\Lambda}$
ρ = density

Subscripts
j = space index
n = time index
o = initial condition
t = time derivative
x = spatial derivative

Superscript
T = transpose

Introduction

ICE protection systems are vital to aircraft safety. Control surfaces, air speed pitot tubes, air intakes, propeller blades, etc., must be protected to prevent ice buildup if the aircraft is to fly in icing conditions. It is important that no ice accumulate on propeller and turbofan blades as this condition could cause a dangerous imbalance that could also result in structural damage when the ice is shed.

Ice protection systems can be broadly classified into two categories 1) anti-icing, and 2) de-icing. Anti-icing systems use chemical or thermal principles to prevent or minimize ice buildup on aircraft surfaces, whereas de-icing systems use a variety of methods to destroy the adhesion of ice accumulations. A de-icer is a device that uses mechanical or thermal methods for removing unwanted ice. The ice removal is generally accomplished either by applying pulses of pressure or electricity. Currently, low performance aircraft commonly use a mechanical de-icing system. This system consists of a strip of rubber applied to a control surface and incorporates ducts which are inflatable by an engine driven compressor. Inflation of the ducts breaks the ice which is then shed by aerodynamic forces. The amount of force generated to expel the ice is a function of the pressure pulse introduced.

The conventional pneumatic de-icer is designed with a stretchable, fabric-reinforced, elastomer surface. This surface is specially compounded for weathering and erosion resistance. When pressurized, the surface distorts considerably, serving to debond the ice under the combined influences of shear, bending, and peel forces. This causes the breakup of the ice cap into pieces as illustrated in Fig. 1. The removal process is completed by the scavenging airstream.

Over the past several years, an advanced type of pneumatic de-icer has been under development. This de-icer is known as the pneumatic impulse ice protection (PIIP) system.[1] The

Presented as Paper 91-0555 at the AIAA 29th Aerospace Sciences Meeting, Reno, NV, Jan. 7–10, 1991; received July 10, 1991; revision received Dec. 8, 1991; accepted for publication Dec. 10, 1991.

*Research Assistant, Mechanical Engineering Department. Student Member AIAA.
†Professor, Mechanical Engineering Department. Associate Fellow AIAA.
‡Professor, Chemical Engineering Department.
§Senior Product Engineer, De-icing Systems.
¶Manager, De-icing Systems. Associate Fellow AIAA.
**Advanced Product Engineer, De-icing Systems.

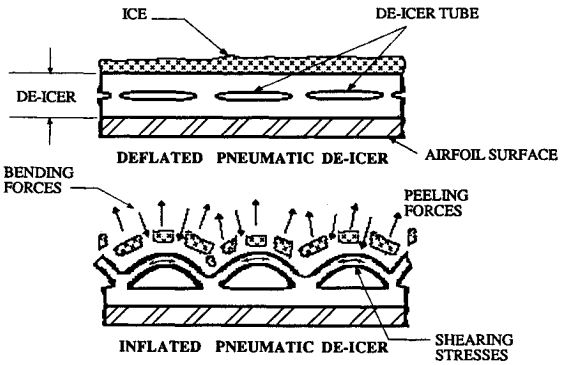

Fig. 1 Conventional pneumatic de-icer.

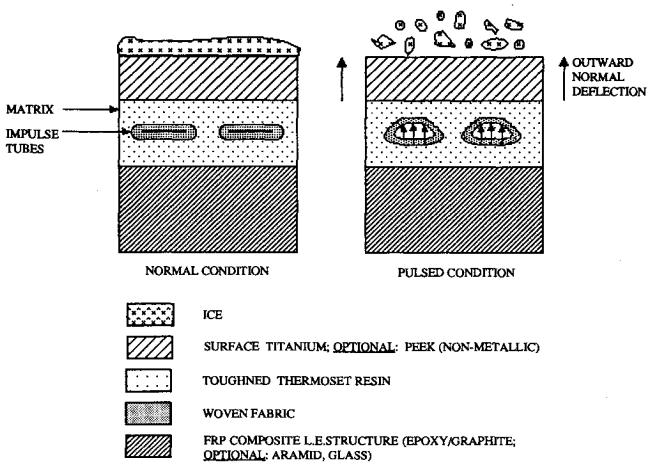

Fig. 2 Pneumatic impulse ice protector construction and operation.

principal reason for this interest is the reduction in the threshold thickness of accreted ice that may be removed by the system. Because of the small size of the ice particles shed, the system may also be utilized as an anti-icer. This new ice-protection system, as illustrated in Fig. 2, relies not only on distortion of the surface to debond accreted ice, but also, on the rapid movement of the surface to launch the ice.

Experiments have shown that surface displacements, typically 0.015–0.030 in., are obtained in as little as 50 μs. The surface itself is a thin titanium alloy (the surface material also may be polyetheretherketone also known as PEEK) overlying a flexible thermoset plastic matrix containing flat fabric-reinforced tubes which, when rapidly pressurized with air, expand slightly, affecting the desired displacement of the surface (Fig. 2).

In this paper, an approximate numerical model of the pneumatic impulse ice protection system is developed. This involves the analysis of transient air flow in the manifold section of the ice protection system. A time dependent, compressible flow model for internal duct flow is utilized. A high resolution shock capturing method, essentially nonoscillatory (ENO) scheme[2] with subcell resolution (SR)[3] and characteristic direction (CD), is used to develop the numerical algorithm. A suitable geometry for enhancing the strength of the shock waves without introducing much stress in the material is given.

Physical Description of the PIIP System

A schematic of the PIIP system is shown in Fig. 3. The source of the impulse is high pressure air (2000 psig nom.). The high-pressure air is either generated with a small compressor or tapped from an existing high pressure system on the aircraft. The air is supplied through small diameter tubing or hose to one or more impulse generation valves, located in the vicinity of the surface to be protected.

For a fixed wing application, the valves would typically be installed behind the leading edge, either fore or aft of the

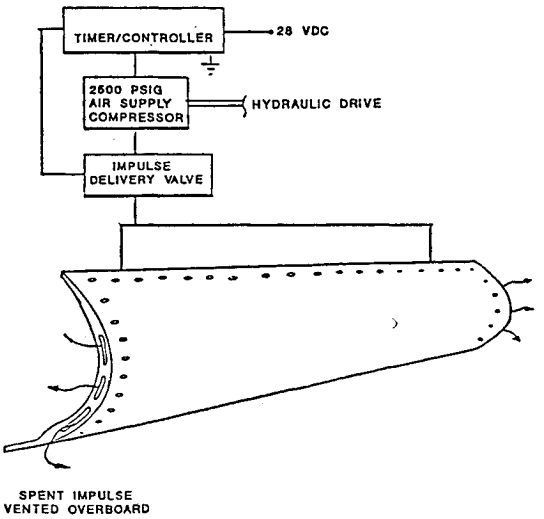

Fig. 3 PIIP system schematic.

front spar. These valves contain a small internal accumulator chamber of predetermined volume, typically less than 1 cubic in. Upon actuation of the valve by a 28 variable direct current (VDC) signal from the controller, the pressurized air in the chamber is discharged extremely rapidly into a port in the back of the leading edge which accesses the de-icer tube. These spanwise tubes, channel the burst of air down the span of the leading edge and overboard to the ambient through vent ports in the back of the leading edge, at the tube ends. The tubes are located adjacent to one another with sufficient number to cover the ice accreting zone of the leading edge.

The rapid pressurization of the impulse tube snaps the surface outward, introducing chordwise tension and bending. The resulting shear stresses developed at the ice-surface interface is the primary source for the debonding of the ice. Also, the rapid outward movement of the surface imparts a sufficient amount of momentum to the ice and a sufficiently large deceleration of the surface, which allows the inertia of the ice to overcome any residual adhesive force.

Numerical Model of the PIIP System

The numerical simulation of the PIIP system (Fig. 4) excludes the timer/controller and the air supply compressor units as shown in Fig. 3. The simulation requires the modeling of airflow inside the system and the geometry of the system. The airflow is modeled as a one-dimensional time-dependent, compressible flow. Accordingly, the inviscid equations of gas dynamics are used as the governing equations. To simulate the geometry of the system, three components, as shown in Fig. 4, were considered: 1) the chamber, 2) the impulse valve, and 3) the de-icer tubing. All three components were coupled together and solved simultaneously, taking into account the wave action occurring inside the chamber.

Chamber Section

The chamber section simulates the internal accumulator chamber of the valve. Therefore, the pressure in this section is assumed constant and is dependent on the compressor operating pressure.

Impulse Valve

The impulse valve is opened and closed on a cycle basis by the discharge of the pressurized air from the chamber. In order to numerically simulate the opening and the closing of the valve, a converging-diverging nozzle whose area varies as a function of time and space (as shown in Fig. 4) is used. The closed and open positions of the valve model are shown in Fig. 5. The change in area of the nozzle, with respect to space and time, makes the flow modeling more difficult as the governing equations include source terms that can make them

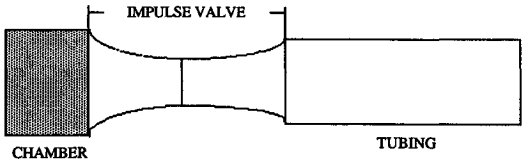

Fig. 4 Numerical model of the PIIP geometry.

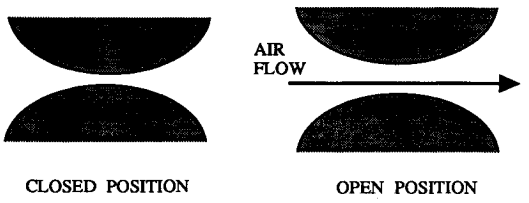

Fig. 5 Impulse valve dynamics.

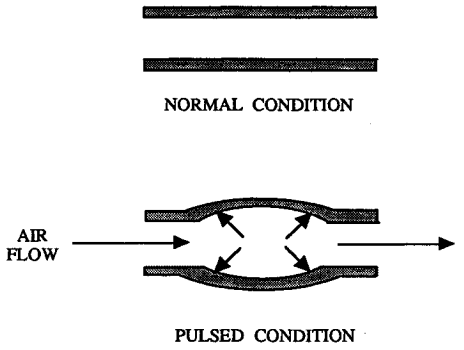

Fig. 6 Tube expansion.

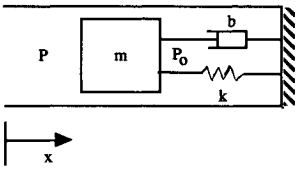

Fig. 7 Second-order, linear model of a real wall.

very stiff. This is one of the reasons for selecting ENO/SRCD as the numerical method to determine the airflow; in the past this method has given accurate solutions for conservation laws with stiff source terms.

De-Icer Tubing

The de-icer tubing is modeled by a straight section. This section undergoes expansion due to the passage of shock waves (Fig. 6). Mathematically, the tubing is modeled as a real wall. A real wall (Fig. 7) is defined here as a wall with mass, damping, and resilience which couples the wall motion to the fluid flow.[4]

An idealized model of a one-dimensional wall of this type is given by a second-order ordinary differential equation describing the motion of the wall

$$m\frac{d^2x}{dt^2} + b\frac{dx}{dt} + k(x - x_o) = A(p - p_o) \qquad (1)$$

where m is the mass of the wall, b is the damping coefficient, k is the spring constant, and A is the area of the wall. The equilibrium position of the wall is x_o, and the pressure outside the wall is p_o, that is assumed constant. If $k = 0$, the model simulates a free piston with or without friction.

Airflow Governing Equations and Boundary Conditions

The inviscid equations of gas dynamics (the Euler equations) are used to simulate the airflow in the PIIP system. The formulation is Eulerian and the equations are written in a conservation form to enable any shock present to be captured without recourse to special treatment. The one-dimensional form of the equations may be written in Cartesian coordinates as

$$U_t + F_x(U) = S(U) \qquad (2)$$

where

$$U = (\rho A, \rho u A, EA)^T$$

$$F(U) = [\rho u A, (p + \rho u^2)A, u(E + p)A]^T$$

$$S(U) = \left(0, p\frac{dA}{dx}, 0\right)^T$$

U is a vector of conserved variables, F is the inviscid flux term, and S is a source vector. The total energy per unit volume E, is expressed as $E = \rho e + \rho u^2/2$, where the specific internal energy e can be obtained from $p = \rho e(\gamma - 1)$. The quantity γ is the ratio of specific heats and is taken to have a constant value of 1.4 for the flows considered. In this study, all properties have been normalized with respect to a reference condition (the upstream stagnation conditions).

Equation (2) can be expressed in a quasilinear form as

$$U_t + A(U)U_x = S(U) \qquad (3)$$

where A is the Jacobian matrix $\partial F/\partial U$. The eigenvalues of the Jacobian matrix $A(U)$ are $\lambda_1 = u$, $\lambda_2 = u + c$, and $\lambda_3 = u - c$ where $c = \sqrt{\gamma p/\rho}$ is the speed of sound. If T and T^{-1} are the right and left eigenvectors of A, it then follows that

$$A = T\Lambda T^1 \qquad (4)$$

$$\Lambda = \text{diag}(\lambda_m) \qquad m = 1, 2, 3 \qquad (5)$$

Since the airflow within the PIIP system involves partial reflection and refraction of shock waves across the boundaries, the boundary conditions require special treatment. The characteristic boundary conditions as described by Pulliam[5] (Fig. 8) are used in this paper. In this method, the eigenvalues of the system (u, $u + c$, and $u - c$) are used to determine which variables are to be calculated, and which must be specified. The variables used at the boundaries are the speed of sound and density.

A major constraint imposed on the analysis, is that the number of boundary values corresponds to the number of incoming characteristics, and that the actual implementation is stable. Eigenvectors of the system are coupled with the chosen fixed boundary values, and one-sided finite differences are used to develop an equation that is solved for flow variables at the boundaries. For supersonic outflow, all information propagates out of the integration domain since u is greater than c, and therefore, a simple extrapolation is sufficient. However, for subsonic outflow, the propagation of information is outside of the integration domain for two of the characteristic variables (u and $u + c$) and into the domain for one variable ($u - c$).

ENO Scheme

The present numerical model is based on an ENO scheme with SR and CD. The essential feature that distinguishes the

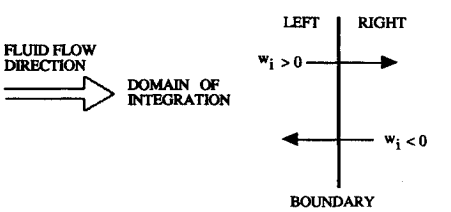

Fig. 8 Propagation of characteristic information at a boundary.

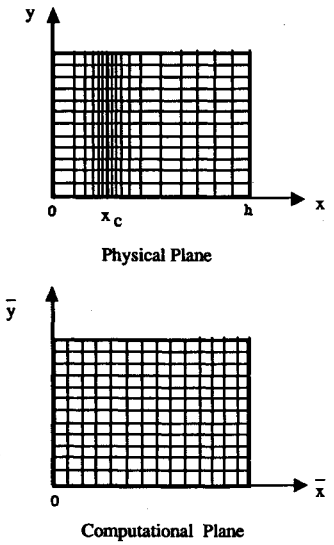

Fig. 9 Transformation of irregular grid into a uniform grid.

ENO construction from other shock capturing schemes is the use of piecewise polynomials to obtain an essentially nonoscillatory reconstruction of the solution from its cell averages. SR is based on the observation that, unlike point values, cell-averages of a discontinuous piecewise-smooth function contain information about the exact location of the discontinuity within the cell. The CD approach improves the resolution of any contact discontinuities for conservation laws with stiff source terms, and helps to improve the quality of the numerical solutions.

The basic ENO scheme with SR, denoted by ENO/SR, achieves significant improvement in the resolution of contact discontinuities. Basically, a good approximation to the locations of discontinuities inside the cell are obtained. The ENO reconstruction technique with SR is used to locate the discontinuity within the cell. Next, the time evolution is accomplished by locally solving the differential equation along each characteristics and advancing in the characteristic direction. This method, which has both the SR and the CD, is denoted by ENO/SRCD. The scheme is described in the Appendix.

Grid Generation

A special grid generation scheme is used to cluster the grid points around the throat of the converging-diverging nozzle. The transformation to refine the mesh about an interior point[6] x_c is shown in Fig. 9 and is given as follows:

$$x = x_c \left\{ 1 + \frac{\sinh[\tau(\bar{x} - B)]}{\sinh(\tau B)} \right\} \tag{6}$$

where

$$B = \frac{1}{2\tau} \ln \left[\frac{1 + (e^{\tau} - 1)(x_c/h)}{1 + (e^{-\tau} - 1)(x_c/h)} \right] \quad \text{for} \quad 0 < \tau < \infty \tag{7}$$

τ is a stretching parameter which varies from zero (no stretching) to large values that produce the most refinement near $x = x_c$.

The metric is given by

$$\frac{\partial \bar{x}}{\partial x} = \frac{\sinh(\tau B)}{\tau x_c \sqrt{1 + (x/x_c - 1)^2 \sinh^2(\tau B)}} \tag{8}$$

where

$$\frac{\partial}{\partial x} = \frac{\partial \bar{x}}{\partial x} \frac{\partial}{\partial \bar{x}} \tag{9}$$

The use of this transformation helped to reduce the computational time.

Results and Discussion

The model was run for two different boundary conditions: 1) open-end conditions, and 2) closed end conditions with a collapsible PIIP surface. The first case was modeled for a system having a length of 6 ft and assuming atmospheric conditions at the exit of the system. For this case, the typical pressure distribution at three different ports for an operating pressure of 1500 psi is shown in Fig. 10. The ports are chosen so that they are located 1 ft from each other and the first port is located 1 ft from the PIIP valve. A peak pressure of 62.5 psi is computed at the location of port 1. The peak pressure drops at ports downstream from the PIIP valve. Also, the compression waves become steeper, and the wave speed increases at locations downstream of the PIIP valve. This phenomena was observed for a range of operating pressures. Figure 11 shows the peak pressures of the three ports for different compressor operating pressures. At an operating pressure of 1500 psi, the drop in peak pressure from port 1 to port 3 is the maximum. Since the impulse generator valve opening of the system is coupled to the compressor pressure, the dynamics of the valve opening dictates the peak pressure at the ports. As the compressor pressure was increased from 1500 psi, the wave profile did not differ from that of 1500 psi. Consequently, 1500 psi is the optimum operating pressure for the geometry used in this study. This optimum operating pressure will differ for different geometries of the valve. Moreover, the exit boundary conditions are also critical to this optimized operating pressure. The wave speeds of the leading compression waves at different locations are given in Fig. 12 for different compressor operating pressures.

For the second case, the open end of the system is replaced by a PIIP surface. The PIIP surface is numerically modeled as a real wall. The deflection of the PIIP surface depends on

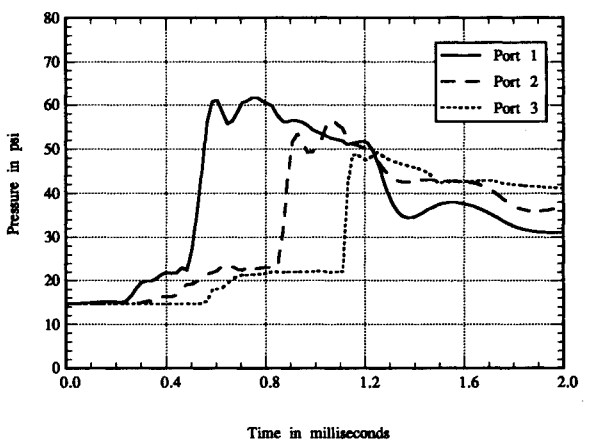

Fig. 10 Pressure distribution for an operating pressure of 1500 psi.

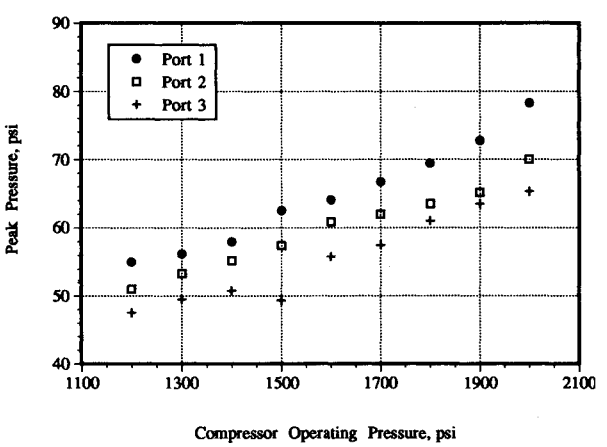

Fig. 11 Peak pressure of the ports for different compressor operating pressures.

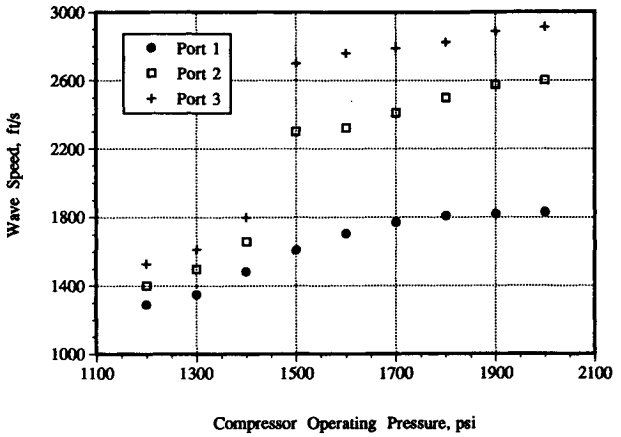

Fig. 12 Wave speeds of compression waves for different compressor pressures.

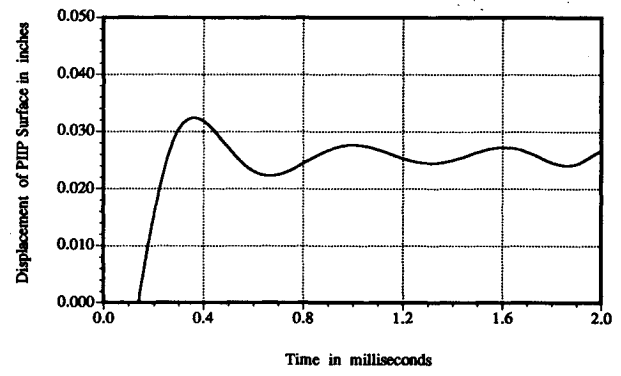

Fig. 13 Typical PIIP surface displacement.

the pressure imparted on the surface. A typical surface displacement is shown in Fig. 13. For this case, the PIIP surface was assumed to be located 1 ft from the impulse valve. This profile was obtained with a compressor pressure of 1500 psi.

For all the calculations presented above, 501 grid points were used. The CPU time per grid point on an IBM/NAS 9080 system was about 10 s.

Conclusions

The main objective of this paper was to numerically model an advanced impulse ice protection system (PIIP). The model based on a high-resolution shock capturing scheme ENO/SRCD, was found to give results of practical use. However, complete agreement with experimental values is yet to be realized. The following steps are being taken to improve the model:

1. An investigation is being undertaken to ascertain that the predicted results are independent of frictional and viscous effects.
2. The surface stresses on the PIIP surface have to be calculated based on the value of the pressure pulse. These surface stresses have to be reduced below the endurance limits, in order to achieve suitable cycle life with acceptable safety margins.
3. Further testing of the model is being pursued with different impulse valve geometries and different manifold cross-sectional shapes.
4. Future modeling will include extending the code to two-dimensions.

Appendix

Construction of the ENO Scheme

A uniform second-order ENO scheme using a reconstruction by means of SR is described in the following algorithm for a nonlinear system of conservation laws of the form given in Eq. (2).

First, the source terms S in Eq. (3) is ignored and the resulting expression is written as

$$U_t + F_x(U) = 0 \tag{A1}$$

with

$$U(x, 0) = U_o(x) \tag{A2}$$

The cell $[x_{j+1/2}, x_{j-1/2}]$ is denoted by I_j. The integration of Eq. (A1) over a cell $(x_{j+1/2}, x_{j-1/2})$ by (t_n, t_{n+1}) leads to

$$\bar{U}_j^{n+1} = \bar{U}_j^n - \frac{\Delta t}{\Delta x}(\hat{F}_{j+1/2} - \hat{F}_{j-1/2}) \tag{A3}$$

where

$$\bar{U}_j^n = \frac{1}{\Delta x}\int_{j-1/2}^{j+1/2} U\, dx \tag{A4}$$

denotes the cell-average of U over the cell I_j at t_n and

$$\hat{F}_{j+1/2} = \frac{1}{\Delta t}\int_0^{\Delta t} F[U(x_{j+1/2}, t_n + \mu)]\, d\mu \tag{A5}$$

denotes the cell boundary value of the flux. In Eq. (A5), the function U in the integral has to be reconstructed from the cell averages $\bar{U}_j^n$. The ENO scheme uses piecewise polynomials to obtain an essentially nonoscillatory reconstruction $U(x, t_n)$ and then uses a local Taylor's series expansion to obtain $U(x, t)$ over (t_n, t_{n+1}).

ENO Reconstruction

At t_n, the numerical solution is assumed to have been obtained as $v^n = \{v_j^n\}$, where $\{v_j^n\}$ represents an approximation to $\bar{U}_j^n$. The $\{v_j^n\}$ is obtained from the numerical scheme

$$v_j^{n+1} = v_j^n - \frac{\Delta t}{\Delta x}(\bar{f}_{j+1/2} - \bar{f}_{j-1/2}) \tag{A6}$$

$$\bar{f}_{j+1/2} = \frac{1}{\Delta t}\int_0^{\Delta t} f[v(x_{j+1/2}, t_n + \mu)]\, d\mu \tag{A7}$$

In order to compute $\bar{f}_{j+1/2}$, v is reconstructed from $\{v_j^n\}$. For a second order scheme, the following procedure is used. A characteristic variable $w^m(x, t_n)$ is constructed from

$$w^m(x, t_n) = l_m(v_j^n)v_i^n, \qquad m = 1, 2, 3 \tag{A8}$$

where $l_m(u)$ denotes the elements of the left-eigenvector T^{-1} of A. The value of i is chosen for each cell I_j such that $j - 2 \le i \le j$ and minimizes the following:

$$|w_{i+2}^n - 2w_{i+1}^n + w_i^n| = \min\{|w_{k+2}^n - 2w_{k+1}^n + w_k^n|: \quad k = j - 2, j - 1, j\} \tag{A9}$$

Note that in Eq. (A8) j is fixed whereas i varies over the points that are relevant to the selection of the stencil for the cell. Thus, the eigenvector of the system should be regarded as a constant system of coordinates.

Let $R_j(x; w^n)$ denote the reconstructed quadratic polynomial over this cell. Then

$$R_j(x; w^n) = a_j + \sigma_j(x - x_j) + C_j(x - x_j)^2 \tag{A10}$$

where

$$C_j = (w_{i+2}^n - 2w_{i+1}^n + w_i^n)/(\Delta x)^2 \tag{A11}$$

$$\sigma_j = (w^n_{i+1} - w^n_i)/\Delta x + (j - i - \tfrac{1}{2})C_j\Delta x \quad \text{(A12)}$$

$$a_j = w^n_j - C_j(\Delta x)^2/24 \quad \text{(A13)}$$

It is possible to select a different stencil for each of the characteristic variables. Now the reconstructed value of v^n_j is given by

$$\tilde{\boldsymbol{R}}_j(x; v^n) = \sum_{k=1}^{3} R_j[x; w^k(v^n_j)]r_k(v^n_j) \quad \text{(A14)}$$

where $r_k(u)$ are the elements of right-eigenvector $\boldsymbol{T}$ and $\boldsymbol{A}$.

Modification by Subcell Resolution

To correct the smearing of linear discontinuities, subcell resolution is introduced into the scheme by modifying its numerical flux. This modification is done in two steps 1) the discontinuity, if any, in the cell $\boldsymbol{I}_j$, is identified; and 2) then the numerical flux in the cells suspected of having a discontinuity is modified by means of a correction term.

To detect a discontinuity in a cell $\boldsymbol{I}_j$, (Note the subcell resolution is used only in the linearly degenerate field [$m = 1$ in Eqs. (A8) and (A15)] in order to improve the resolution of discontinuities. For more information, refer to Harten's original work on ENO/SR scheme)[3]

$$F_j(z) = \frac{1}{\Delta x} l_1(v^n_j)\left[\int_{x_{j-1/2}}^{z} \tilde{\boldsymbol{R}}_{j-1}(x; v^n)\,dx + \int_{z}^{x_{j+1/2}} \tilde{\boldsymbol{R}}_{j+1}(x; v^n)\,dx\right] - v^n_j \quad \text{(A15)}$$

If

$$|\sigma_j| > |\sigma_{j-1}| \quad \text{(A16)}$$

$$|\sigma_j| \geq |\sigma_{j+1}| \quad \text{(A17)}$$

$$F_j(x_{j-1/2})F_j(x_{j+1/2}) \leq 0 \quad \text{(A18)}$$

a discontinuity is considered to be located at θ_j in the cell, satisfying

$$F_j(\theta_j) = 0 \quad \text{(A19)}$$

The location of θ_j can then be approximated by using any standard root-finding method. The bisection method is used here. The characteristic speed of the linearly degenerate field is the flow velocity u, which can differ in sign in different regions of the field. To make the programming easier, the numerical flux is calculated in two stages. First, evaluate for all j

$$\tilde{f}_{j+1/2} = \tilde{f}^{\text{ENO}}_{j+1/2} = f^R(v^L_{j+1/2}, v^R_{j+1/2}) \quad \text{(A20)}$$

where $f^R(v_1, v_2)$ is an approximation to the flux at the origin in a Riemann problem with u_1 to the left, and u_2 to the right:

$$v^L_{j+1/2} = v^n_j + \Delta x\left(1 - \frac{\Delta t}{\Delta x}A_j\right)\frac{\sigma_j}{2} \quad \text{(A21)}$$

$$v^R_{j+1/2} = v^n_{j+1} - \Delta x\left(1 + \frac{\Delta t}{\Delta x}A_{j+1}\right)\frac{\sigma_{j+1}}{2} \quad \text{(A22)}$$

Then, sweep over the mesh again and collect the contribution of each cell to the correction terms to the numerical flux, i.e., if

$$u^n_j > 0$$

then

$$\tilde{f}_{j+1/2} = \tilde{f}_{j+1/2} + \frac{1}{\Delta t}\,\mathrm{d}_j\,(x_{j+1/2} - u^n_j\Delta t, x_{j+1/2})r_1(v^n_j) \quad \text{(A23)}$$

or if

$$u^n_j \leq 0$$

then

$$\tilde{f}_{j-1/2} = \tilde{f}_{j-1/2} - \frac{1}{\Delta t}\,\mathrm{d}_j\,(x_{j-1/2}, x_{j-1/2} - u^n_j\Delta t)r_1(v^n_j) \quad \text{(A24)}$$

where

$$\mathrm{d}_j\,(y_1, y_2) = \int_{y_1}^{y_2} l_1(v^n_j)[\boldsymbol{R}_j(x; v^n) - \boldsymbol{L}_j(x; v^n)]\,dx \quad \text{(A25)}$$

$\boldsymbol{L}_j(x; v^n)$ is a polynomial of degree $(r - 1)$ which reconstructs v^n to $O(h^r)$ and r is the desired order of accuracy of the scheme. In this study, $r = 2$ is used.

If the discontinuity condition, as specified in Eqs. (A16–A19) is satisfied, then define a product

for $u^n_j > 0$

$$F_p = F_j(x_{j+1/2})F_j(x_{j+1/2} - u^n_j\Delta t) \quad \text{(A26)}$$

$$h_j = \begin{cases} c_{j+1/2}(x_{j+1/2} - u^n_j\Delta t, x_{j+1/2}) & \text{if } F_p > 0 \\ c_{j-1/2}(x_{j-1/2}, x_{j-1/2} - u^n_j\Delta t) & \text{if } F_p \leq 0 \end{cases} \quad \text{(A27)}$$

$$\tilde{f}_{j+1/2} = \tilde{f}_{j+1/2} + \frac{1}{\Delta t}h_j r_1(v^n_j) \quad \text{(A28)}$$

or if $u^n_j \leq 0$

$$F_m = F_j(x_{j+1/2})F_j(x_{j-1/2} - u^n_j\Delta t) \quad \text{(A29)}$$

$$h_j = \begin{cases} c_{j+1/2}(x_{j-1/2} - u^n_j\Delta t, x_{j+1/2}) & \text{if } F_m > 0 \\ c_{j-1/2}(x_{j-1/2}, x_{j-1/2} - u^n_j\Delta t) & \text{if } F_m \leq 0 \end{cases} \quad \text{(A30)}$$

$$\tilde{f}_{j-1/2} = \tilde{f}_{j-1/2} + \frac{1}{\Delta t}h_j r_1(v^n_j) \quad \text{(A31)}$$

$$c_{m+1/2}(y_1, y_2) = \int_{y_1}^{y_2} l_1(v^n_j)[\boldsymbol{R}_{m+1}(x, v^n) - \boldsymbol{R}_m(x, v^n)]\,dx$$

$$\text{for} \quad m = j - 1, j \quad \text{(A32)}$$

Time Evolution and Cell Averaging

Using a Taylor's series expansion, Eqs. (A1) and (A2) can be written as

$$\boldsymbol{U}(x_o + \boldsymbol{A}\Delta t, \Delta t) = \boldsymbol{U}(x_o, 0) + \frac{\partial \boldsymbol{U}}{\partial x}(\boldsymbol{A}\Delta t) + \frac{\partial \boldsymbol{U}}{\partial t}(\Delta t) + \cdots \quad \text{(A33)}$$

$$\boldsymbol{U}(x_o + \boldsymbol{A}\Delta t, \Delta t) - \boldsymbol{U}(x_o, 0) = \Delta t\left[\boldsymbol{A}\frac{\partial \boldsymbol{U}}{\partial x} + \frac{\partial \boldsymbol{U}}{\partial t}\right] \quad \text{(A34)}$$

$$\boldsymbol{U}(x_o + \boldsymbol{A}\Delta t, \Delta t) - \boldsymbol{U}(x_o, 0) = \Delta t\left[\frac{\partial \boldsymbol{F}}{\partial \boldsymbol{U}}\frac{\partial \boldsymbol{U}}{\partial x} + \frac{\partial \boldsymbol{U}}{\partial t}\right] \quad \text{(A35)}$$

$$\boldsymbol{U}(x_o + \boldsymbol{A}\Delta t, \Delta t) - \boldsymbol{U}(x_o, 0) = \Delta t[\boldsymbol{S}(\boldsymbol{U})] \quad \text{(A36)}$$

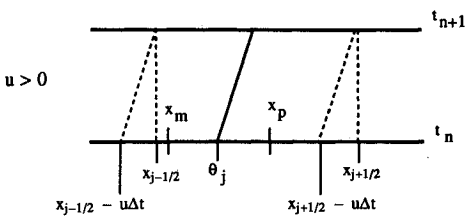

Fig. A1 Time evolution.

Therefore

$$\frac{U(x_o + A\Delta t, \Delta t) - U(x_o, 0)}{\Delta t} = S(U) \qquad \text{(A37)}$$

or

$$\frac{\mathrm{d}}{\mathrm{d}t} U_o(x_o + A\Delta t, \Delta t) = S(U_o + A\Delta t, \Delta t) \qquad \text{(A38)}$$

The solution to Eq. (2) evolves according to the ODE, Eq. (A38), along the characteristics $x = x_o + u\Delta t$.

If there is a discontinuity at θ_j inside the cell $I_j(x_{j-1/2}, x_{j+1/2})$ with $\theta_j \le x_{j+1/2} - u\Delta t$ as shown in Fig. A1, at t^n time level, $\tilde{v}^n_{j-1}$ is used as the solution to the left of θ_j and, $\tilde{v}^n_{j+1}$ to the right of θ_j. Since the solution to Eq. (A38) evolves along the characteristics, approximate solution values at t_{n+1} level can be obtained by solving Eq. (A38) and advancing in the characteristic direction. If $q(x, t_{n+1})$ denotes the solution of Eq. (A38) at t_{n+1} over $(x_{j-1/2}, x_{j+1/2})$, obtained by using the initial values $\tilde{v}^n_{j-1}$ on $(x_{j-1/2} - u\Delta t, \theta_j)$ and $\tilde{v}^n_{j+1}$ on $(\theta_j, x_{j+1/2} - u\Delta t)$, the numerical solution v^{n+1}_j is then an approximation to

$$\frac{1}{\Delta x}\int_{x_{j-1/2}-u\Delta t}^{\theta_j} q(x, t_{n+1})\,\mathrm{d}x + \int_{\theta_j}^{x_{j+1/2}-u\Delta t} q(x, t_{n+1})\,\mathrm{d}x$$

Using x_m and x_p, the midpoints in the intervals $(x_{j-1/2} - u\Delta t, \theta_j)$ and $(\theta_j, x_{j+1/2} - u\Delta t)$ respectively, (Fig. A1) compute v^{n+1}_j from a modified Euler's method as follows:

$$q^*_m = \tilde{v}^n_{j-1} + \Delta t S[\tilde{R}_{j-1}(x_m; v^n)] \qquad \text{(A39)}$$

$$q^*_p = \tilde{v}^n_{j+1} + \Delta t S[\tilde{R}_{j+1}(x_p; v^n)] \qquad \text{(A40)}$$

$$q_m = \tilde{v}^n_{j-1} + \frac{\Delta t}{2}\{S[\tilde{R}_{j-1}(x_m; v^n)] + S(w^*_m)\} \qquad \text{(A41)}$$

$$q_p = \tilde{v}^n_{j+1} + \frac{\Delta t}{2}\{S[\tilde{R}_{j+1}(x_p; v^n)] + S(w^*_p)\} \qquad \text{(A42)}$$

Other locations of θ_j and cases with regions without discontinuities can be treated similarly. The time loop of the algorithm is closed by taking the cell averages of the solution.

References

[1]Martin, C., and Putt, J., "An Advanced Pneumatic Impulse Ice Protection System (PIIP) for Aircraft," AIAA 28th Aerospace Sciences Meeting, AIAA-90-0492, Reno, NV, Jan. 1990.

[2]Harten, A., Engquist, B., Osher, S., and Chakravarthy, S. R., "Uniformly High Order Accurate Essentially Non-Oscillatory Schemes III," *Journal of Computational Physics*, Vol. 71, No. 2, 1987, pp. 231–303.

[3]Harten, A., "ENO Schemes with Subcell Resolution," *Journal of Computational Physics*, Vol. 83, No. 1, 1989, pp. 148–184.

[4]Katz, I. M., and Shaugnessy, E. J., "Computer Aided Analysis of 1-D Compressible Flow Problems in a Lagrangian Particle Description Using the α Method," *Computers and Fluids*, Vol. 18, No. 2, 1990, pp. 75–101.

[5]Pulliam, T. H., "Characteristic Boundary Conditions for the Euler Equations," *Numerical Boundary Conditions Proceedings*, NASA CP-2201, 1981, pp. 165–181.

[6]Anderson, D., Tannehill, J. C., and Pletcher, R. H., *Computational Fluid Mechanics and Heat Transfer*, Hemisphere, Washington DC, 1984, pp. 250–251.